PAPER

A repeatable and scalable fabrication method for sharp, hollow silicon microneedles

IOP Publishing Journal of Micromechanics and Microengineering
J. Micromech. Microeng. **28** (2018) 035007 (13pp) https://doi.org/10.1088/1361-6439/aaa6a8

A repeatable and scalable fabrication method for sharp, hollow silicon microneedles

H Kim[1], L S Theogarajan[2] and S Pennathur[1]

[1] Mechanical Engineering Department, University of California—Santa Barbara, Santa Barbara, CA 93106, United States of America
[2] Electrical and Computer Engineering Department, University of California—Santa Barbara, Santa Barbara, CA 93106, United States of America

E-mail: hkim00@umail.ucsb.edu

Received 19 August 2017, revised 11 December 2017
Accepted for publication 10 January 2018
Published 31 January 2018

Abstract

Scalability and manufacturability are impeding the mass commercialization of microneedles in the medical field. Specifically, microneedle geometries need to be sharp, beveled, and completely controllable, difficult to achieve with microelectromechanical fabrication techniques. In this work, we performed a parametric study using silicon etch chemistries to optimize the fabrication of scalable and manufacturable beveled silicon hollow microneedles. We theoretically verified our parametric results with diffusion reaction equations and created a design guideline for a various set of miconeedles (80–160 μm needle base width, 100–1000 μm pitch, 40–50 μm inner bore diameter, and 150–350 μm height) to show the repeatability, scalability, and manufacturability of our process. As a result, hollow silicon microneedles with any dimensions can be fabricated with less than 2% non-uniformity across a wafer and 5% deviation between different processes. The key to achieving such high uniformity and consistency is a non-agitated HF-HNO_3 bath, silicon nitride masks, and surrounding silicon filler materials with well-defined dimensions. Our proposed method is non-labor intensive, well defined by theory, and straightforward for wafer scale mass production, opening doors to a plethora of potential medical and biosensing applications.

Keywords: microneedles, fabrication, HF-HNO_3, silicon

(Some figures may appear in colour only in the online journal)

1. Introduction

Hypodermic needles have been an unpleasant necessity in the medical industry for a while, due to the discomfort, phobia, and potential for transmission of bloodborne pathogens. Luckily, over the last few decades, engineers and scientists have developed other methods to extract fluid or deliver drugs into the body using oral delivery and/or transdermal delivery methods, or by developing smaller, less painful microneedles. Specifically, microneedles are of interest due to the potential ease of fabrication and manufacturing, as well as their ability to deliver and extract fluid with the same efficacy as hypodermic needles [1].

In addition to the plethora of research into the fabrication of microneedles, the last decade has seen the commercialization of microneedles such as the Microstructured Transdermal System by 3M, Dermaroller, Macroflux, Micro-trans, H-patch, MicronJet, Nanoject, and Soluvia [2, 3]. Dermaroller is the first commercialized microneedle-based product to enhance skin texture or to treat scars [4]. Other devices, such as Soluvia and MicronJet, are designed for vaccination or drug delivery purposes using microneedles that are connected to a plastic adapter or syringes [5]. These commercialized products are typically fabricated by industrial microelectromechanical system (MEMS) technologies [6–8], micromachining [9], and micromolding [10]. Although all these products are already

on the market, there is still a growing need for efficient and reliable micromanufacturing methods of microneedles for different materials with enhanced scalability and repeatability for the hundreds of other applications in the medical field.

To address this crucial need, researchers have more recently been innovating different manufacturing methods for microneedle fabrication. For example, drawing lithography relies on either UV irradiation [11] or high temperature [12] to rapidly produce a microneedle array, with needle dimensions controlled by varying the curing or heating time and the volume of the polymeric material. However, drawing lithography cannot easily achieve a sub mm range of needle pitch as it must be large enough to avoid the overlap of the solution in the UV irradiation [11]. To overcome these obstacles, researchers enhanced the scalability and controllability of UV lithography through spatial control [13] and integrating a rotating prism [14], in which the needle dimension is adequately controlled by adjusting the distance between the light and UV-sensitive solution and doses of UV exposure. Although UV lithography does not require thermal baking that can induce mechanical and thermal stress, the minimum pitch between the microneedles needs to be larger than the twice the needle base diameter to avoid any overlap of UV exposure [13, 14], which limits the freedom of array design.

Other methods to fabricate microneedles include droplet-born air blowing (DAB), micromolding, and MEMS-based technologies [6–8]. The DAB method is a less aggressive method than the above techniques as it does not require heat or UV irradiation [15]. Thus heat-sensitive biological drugs can be formed into dissolvable microneedles using DAB in a controllable and reliable fashion. Micromolding is another approach that can create dissolvable [16] or ceramic [17] microneedles repeatedly at low cost, but neither method is yet a truly reliable technique.

Additionally, there have been many efforts to fabricate arrays of microneedles using MEMS techniques with a wide variety of materials, such as stainless steel [18], gold [19, 20], biodegradable polymer [21], and glass [22]. Among these materials, silicon is widely adopted due to its availability, low cost, material properties, and ease of fabrication for simple [23–26] or complex structures [27]. Silicon microneedles, however, generally either do not satisfy both the scalability and manufacturability required for mass production or are not effective for skin insertion. To satisfy the preceding criteria, silicon microneedles must have the following design specifications: (1) an appropriate base to height ratio (to achieve the mechanical strength required pierce skin efficiently [28]), (2) a beveled tip (to avoid clogging of fluid [29]), (3) appropriate needle height (to effectively deliver drug and/or monitor biomarkers as the skin thickness can differ [30]), and (4) high uniformity with polished surface (to ensure low skin insertion force [31]).

Therefore, here we report a fabrication method with high uniformity, scalability, and repeatability for creating uniform hollow and solid silicon microneedles with sharp beveled tips. The scalability of the process is accomplished through photolithography techniques, where we can design and fabricate hollow microneedles with versatile, consistent dimensions. We also enhanced the repeatability by designing a silicon structure in a way that only the needle tip width sharpens consistently without altering the needle base width, height, and pitch in a non-agitated acidic bath during the final step of the fabrication. Due to the non-disturbed etch system, we can achieve 98% uniformity across a single silicon wafer and predict the final microneedle dimensions by using a simple diffusion-reaction equation with no added convection, further improving our fabrication controllability. We performed a parametric study on etchant volume, composition, and geometries of silicon structures and outlined design guidelines with which to repeatedly and reliably create microneedles with base width 80–160 μm, array pitch 100–1000 μm, inner bore diameter 40–50 μm, and height 150–350 μm geometries. Due to our non-labor intensive wet etching technique, the setup is far less complicated and less time-consuming than other conventional dry and wet etching methods, and this process enables freedom in designing a broad range of microneedle features and successfully translates the initial design to the final product. Due to its repeatability, uniformity, and scalability, our fabrication process provides a potential promise for mass production of hollow and solid silicon microneedles.

2. Fabrication

2.1. Fabrication overview

Hollow silicon microneedles are typically fabricated using dry [23, 26, 27] or a combination of dry and wet etching techniques [24, 25, 32], in which an inner bore is created by a plasma of reactive gases while acid etchants form the overall shape of the microneedle. These fabrication techniques, however, do not have absolute control of the individual dimensions, such as base width, height, and pitch, nor can they be amenable to mass production. For example, a dry etching system, despite its excellent control of dimensions and uniformity, lacks manufacturability due to the resulting rough surfaces when using an inductively coupled plasma (ICP) [24]; this rough surface can increase the skin insertion forces due to an undesirable friction between the skin and needle surfaces [30]. Deep reactive ion etching (DRIE) can improve the surface roughness, etch rate, and resolution, but achieving microneedle arrays of wide pitch can be difficult due to negative re-entrant profiles that are unavoidable when etching a large open area [33]. As for the wet etching systems, silicon can be etched either in isotopic or anisotropic fashion depending on the nature of the etchant. Potassium hydroxide (KOH) etching, the most commonly used etchant to create solid silicon microneedles, is virtually impossible for scalable array fabrication in a hollow form because of the dependence on wafer orientation [34]. Unlike KOH etching, a mixture of hydrofluoric acid (HF) and nitric acid (HNO_3) is independent of the wafer orientation and, combined with dicing allows for a wider range of microneedle pitch to height ratios [35]. Unfortunately, for these microneedles, agitating is necessary to achieve a sharp microneedle tip as the silicon is etched in every direction. The agitation, however, makes the process unrepeatable, hard to control, and non-uniform across a wafer [35, 36], lowering

the possibility of mass production [37]. Furthermore, when Mukerjee and co-workers [11] alternated between agitation and non-agitation of the etchant to laterally impose a directional bias to sharpen the microneedle tip, both microneedle height and base were etched during the quiescent phase, leading to a detrimental, non-uniform microneedle shapes. Stoeber [10] also used non-agitated isotropic acid etchant to polish the surface, but microneedle base was etched during this step which can lead to geometric variation from the initial design. To overcome these limitations, we have incorporated a novel needle design and modified a conventional wet etch system to ensure high repeatability, uniformity, and controllability of the fabrication process.

Specifically, our needle base width and pitch are first defined by a photolithography step, and the needle height and inner bore are defined by the use of DRIE. We create our structures through photolithography and DRIE rather than dicing [36, 38] to increase the scalability of the process and design control for creating hollow microneedles. For example, we can easily achieve a beveled tip because our structures are fabricated with hollow bores that are offset from the center of the needles by several tens of micrometers. Depending on the offset and size of the inner bore, we can effectively alter the final shape of the microneedle to avoid skin clogging and improve the sharpness of the needle tip. The resulting silicon structures after the dry etching consist an array of square columns (pillars), and a single pillar is surrounded by narrower and thinner columns (fillers) which act as sacrificial structures for a future wet etching process. Due these fillers that are closely located from one another, we can avoid the negative re-entrant profiles when etching an array of tall needles with a wide pitch in a DRIE system. Furthermore, these fillers impose a directional bias in our final step during the wet etch, allowing only the needle tip to sharpen in the process. This acid etchant (HF-HNO_3) in the final fabrication step is appropriate for mass scale production because the etchant can polish the silicon surface while sharpening the needle tip in a multi-wafer scale [39]. Since we do not agitate the solution, our method is less labor intensive and has low of process variations compared to the conventional method [36], giving high repeatability rate between the processes when fabricating multiple microneedle arrays of the same dimensions. Also, a non-disturbed bath has no variation in temperature, activation energy, or flow rate like the conventional method [38]. This controllable constant temperature etch can be modeled with simple diffusion reaction equations, which allows our fabrication to be repeatable and consistent.

2.2. Fabrication details

The fabrication method, summarized in figure 1, starts with a silicon wafer that is 500 μm thick double-sided-polished (N-type, resistivity 1–100 Ω cm) and 4″ in diameter. To create arrays of hollow microneedles of 250 μm in height, 140 μm in base width, 1 mm in pitch, and 40 μm in borehole diameter, a 3 μm thick silicon dioxide (SiO_2) and a 2 μm thick low-stress silicon nitride (Si_3N_4) films are deposited via plasma enhanced chemical vapor deposition (PECVD) on each side of the wafer as shown in figure 1(a). 4 × 4 arrays of square dies, in which a single die consists of 13 × 13 arrays of circles of 40 μm in diameter (to eventually be the hollow bore of the microneedle), are patterned onto the 3 μm SiO_2 film. It should be noted that the borehole diameter, pitch, and base width can be controlled at the micron-scale through appropriate mask design. For this patterning step, we spin-coat an adhesive primer (MCC Primer 80/20, MicroChem, Newton, MA, USA) at 4000 rpm for 30 seconds and soft bake at 115 °C for 2 min on a hot plate. AZ4620 positive photoresist (AZ Electronic Materials, Somerville, NJ) is then spin coated at 2500 rpm for 40 seconds and baked at 110 °C for 10 min. After exposing the pattern to UV light with an intensity of 18.5 mW cm^{-2} for 26 seconds, the features are developed in AZ400K (1:3) for 3–4 min. The SiO_2 film is then etched in an ICP etcher (Pressure = 0.5 Pa, RF/ICP power = 50/900 W, CF_4/CHF_3 flow-rate = 30/10 sccm) to expose the silicon underneath (figure 1(b)). Using AZ4620 and SiO_2 as a hard mask, the exposed silicon bores are etched through the wafer using a standard Bosch process in a deep reactive-ion etcher (DRIE), resulting in the average etch rate of 1.6 μm min^{-1} (figure 1(c)). The Si_3N_4 film on the bottom acts as an etch stop to ensure that the holes are uniformly etched through. Next, squares are patterned onto the Si_3N_4 film (the pillar and fillers), in which a single 140 μm wide square (pillar) is surrounded by approximately 800 of 10 μm wide squares (fillers). These 140 μm wide squares are placed 20 μm off-centered from the center of the circle to create beveled tips. We again perform lithography and ICP etching as mentioned previously (figure 1(d)). The standard Bosch process creates the high-aspect-ratio square columns with the average etch rate of 2.3 μm min^{-1} (figure 1(e)). Any desirable microneedle height can be achieved by controlling the total dry etching time during this DRIE process.

To sharpen the needle tip, we introduce a mixture of HF and HNO_3. The etch solution is prepared by mixing HF (49 wt%) and HNO_3 (69 wt%) in 1:19 by volume ratio into a high-density polyethylene (HDPE) bottle. We chose this ratio (rich-HNO_3) to guarantee a stable etch since HNO_3 is known to stabilize etchants as compared to a highly reactive etchant such as HF. Furthermore, a high concentration of HNO_3 ensures a generally constant temperature during the etch, since it is the reactivity of the HF that causes the temperature rise [39]. The bottom of the wafer is covered with a Teflon tape to ensure that no etchant seeps into the holes. During the wet etching process, the non-disturbed etchant sharpens the pillar tip laterally from the edge [40] and etches the surrounding filler material vertically. The pillar height remains constant throughout the etch due to the Si_3N_4 hard mask that is on top of the pillar. After a carefully timed etch (±1 min) at room temperature without agitation, the array of beveled silicon microneedles with an off-centered hole is complete (figure 2).

3. Results

With our repeatable fabrication method, we achieve arrays of hollow microneedles at the wafer scale that is highly uniform and meets our initial design requirements. Figure 3 shows

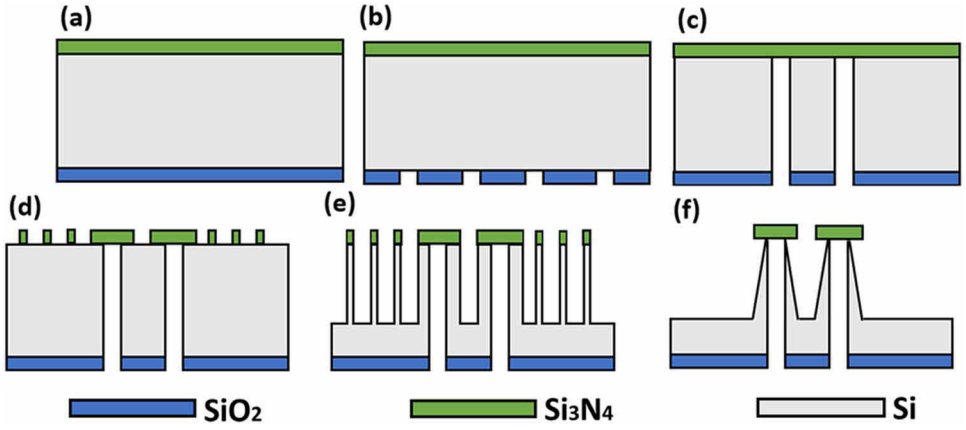

Figure 1. Schematic illustration of the hollow microneedle fabrication process: (a) deposition of 3 μm silicon oxide (SiO_2) and 500 nm silicon nitride (Si_3N_4); (b) dry etching of SiO_2 circular holes of 40–50 μm in diameter; (c) DRIE of holes through the 500 μm thick wafer; (d) dry etching of Si_3N_4 square patterns width ranging from 80 to 160 μm for desirable needle base width, surrounded by the 10–20 μm squares that will be fillers; (e) DRIE of 150–350 μm tall 13 $\times$ 13 cm pillar array with spacing ranging from 50 to 1000 μm. (f) Wet etching using hydrofluoric acid and nitric acid to sharpen the tip and reveal the hole. When the tip sharpens, the silicon nitride mask falls off.

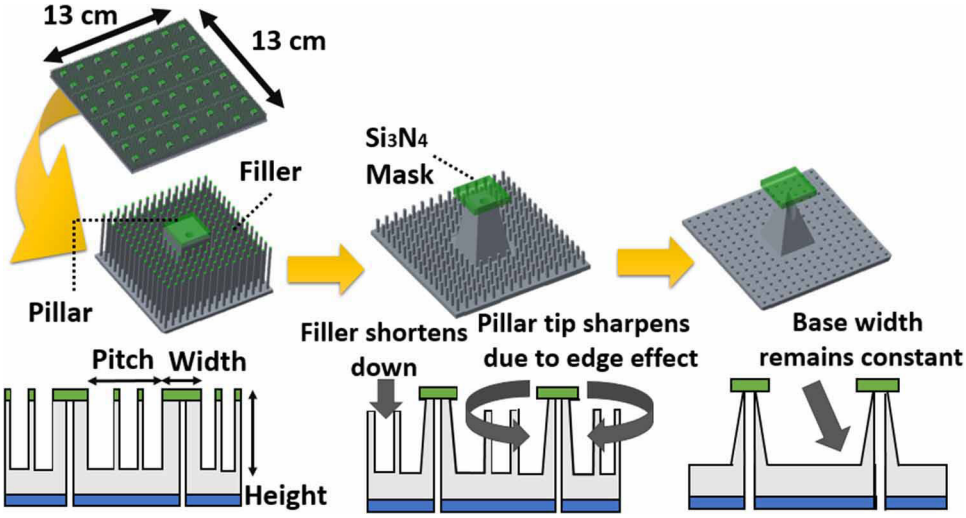

Figure 2. Schematic illustration of the non-agitated (HF-HNO_3) bath sharpening mechanism with fillers.

the final sharp, hollow, beveled microneedles with a less than average of 2% geometric variation in height, width, and pitch of both pillars and fillers across a typical wafer. We initially designed the microneedle to be sharp and beveled with 1 mm in pitch, 140 μm in base width, 250 μm in height, and 40 μm in borehole diameter, and our final needle geometries are close to perfect from our original design. We chose these dimensions to ensure mechanical stability and repeatable puncture of the epidermis layer (221 μm deep in the finger [41]). Note that the non-uniformity between the five processes for creating an identical microneedle profile is around 5% (see section 3.2). Among these processes, 3 batches were fabricated in a wafer scale, and these microneedles were 1 mm in pitch, 160 μm in base width, and approximately 250 μm in height.

The key to building consistent microneedle arrays with a sharp tip is having a well-controlled etch rate and not etching the base and height of the pillar. We achieve this by adopting a non-agitated bath, a silicon nitride mask, and a well-defined set of filler materials in between the pillars. To fabricate the sharpest and most repeatable microneedle arrays, we systematically varied etch chemistry ratio, etchant volume, and silicon microstructure geometry, such as the pillar pitch, filler density, and filler surface area, to find how each parameter affected the final design. Given our findings, we can not only predict the settings needed to produce repeatable and reliable microneedles but also are able to provide design guidelines for wafer scale fabrication of hollow silicon microneedles with needle base width ranging from 80 to 160 μm, array pitch 100–1000 μm, inner bore diameter 40–50 μm, and height 150–350 μm. It should be noted that we can achieve any dimensions that are outside of the range listed the above as it was chosen to simplify our parametric study significantly. Hollow silicon microneedles with different heights are shown in figure 4, and we can achieve needle height greater than 350 μm with a silicon substrate that is thicker than 500 μm.

3.1. Effect of etch chemistries

The etch rate depends on both the total etchant volume with respect to the mass of silicon being etched (figure 5) as well as the volumetric ratio of etchants HF to HNO_3 (figure 6). We found that the etch rate is sensitive to both etchant volume

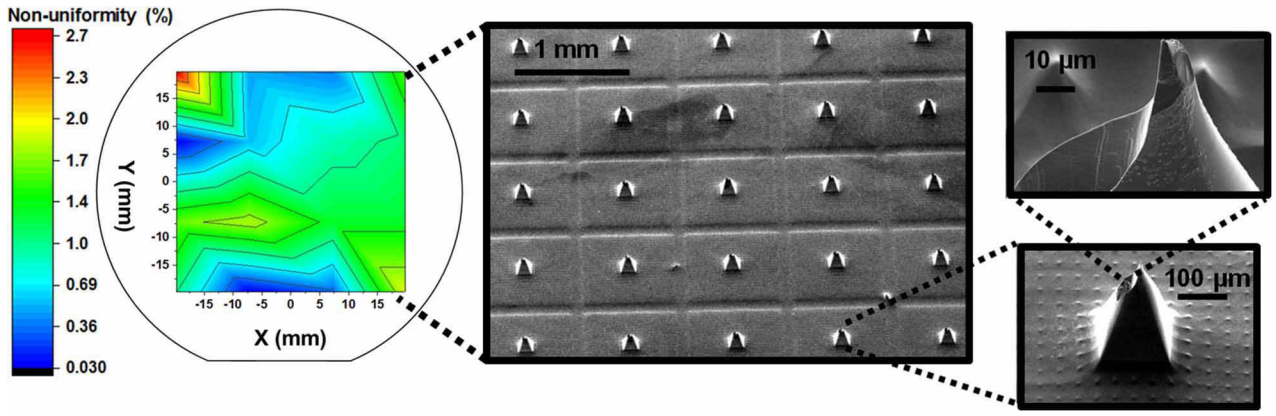

Figure 3. (Left) A representation of the non-uniformity of each individual 13 × 13 mm die as compared to the average of the center pillar tip width. The array to array non-uniformity is 1.47 ± 0.51% across a typical wafer. The nonuniformity rate was calculated by dividing the standard deviation with respect to the mean and multiplying it by 100 [38]. Within an array, the non-uniformity of needle base width and height is 1.41 and 1.45% respectively. Note that in this particular wafer, each 13 × 13 mm die contained roughly 169 microneedles, spaced 1 mm apart. There were approximately 800 fillers of 10 μm in width. (Right) SEM of a silicon microneedle array showing sharp, consistent needle tips with 1 mm in pitch, 140 μm in base width, 250 μm in height, and 40 μm in borehole diameter. A close up of needle tip, showing the offset hole to create the bevel. The tip width of μm should effectively puncture the skin at any location.

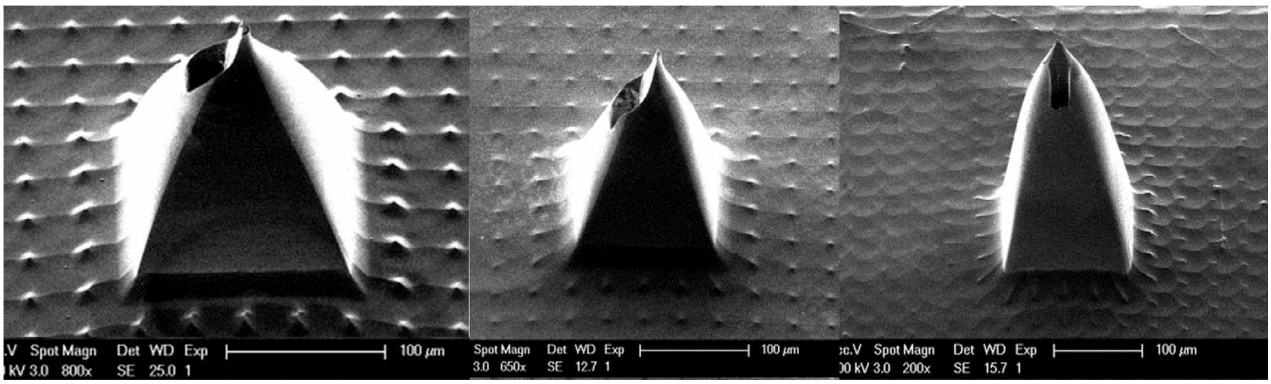

Figure 4. SEM images of hollow microneedles with height ranging from 200, 250, and 350 μm with inner bore diameter of 40 μm and base width of 140 μm.

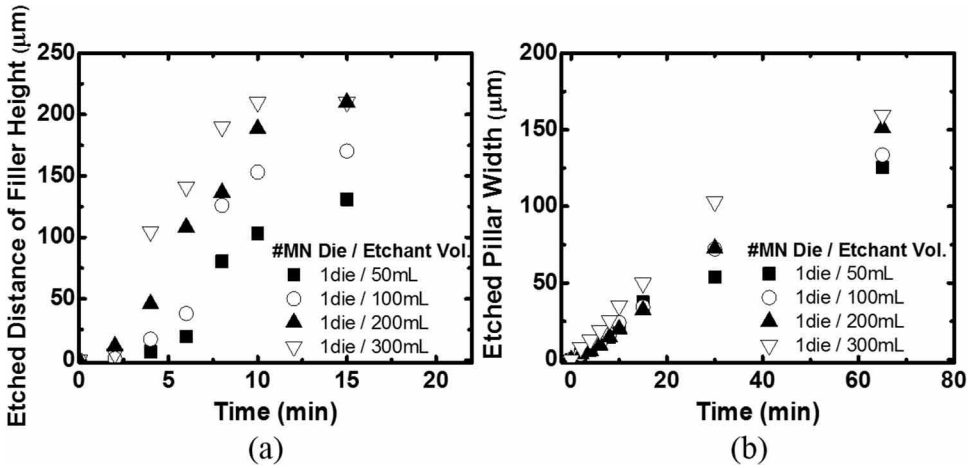

Figure 5. (a) The etched distance of filler height with respect to time. (b) Etched pillar width with respect to time. One die consisted an array of 13 × 13 microneedles of 160 μm in width and 200 μm in height that was 1 mm apart from each other. There were 700 fillers of 10 μm in width surrounding a single pillar. The etchant volume of HF (49 wt%): HNO_3 (69 wt%) in volume ratio of 1:19 was varied from 50 to 300 ml for a single die of microneedle array, which was approximately 0.02 g of silicon.

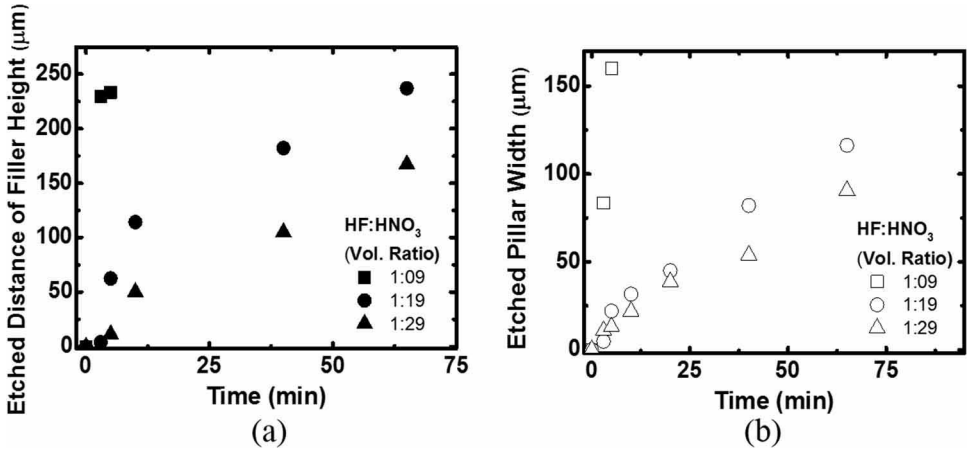

Figure 6. (a) The etched distance of filler height with respect to time. (b) Etched pillar width with respect to time. One die consisted an array of 13 × 13 microneedles of 160 μm in width and 250 μm in height that was 1 mm apart from each other. There were 700 fillers of 10 μm in width surrounding a single pillar. The volume ratio of HF (49 wt%): HNO_3 (69 wt%) was varied from 1:9 to 1:29, and the total etchant volume was 50 ml for etching 0.02 g of silicon.

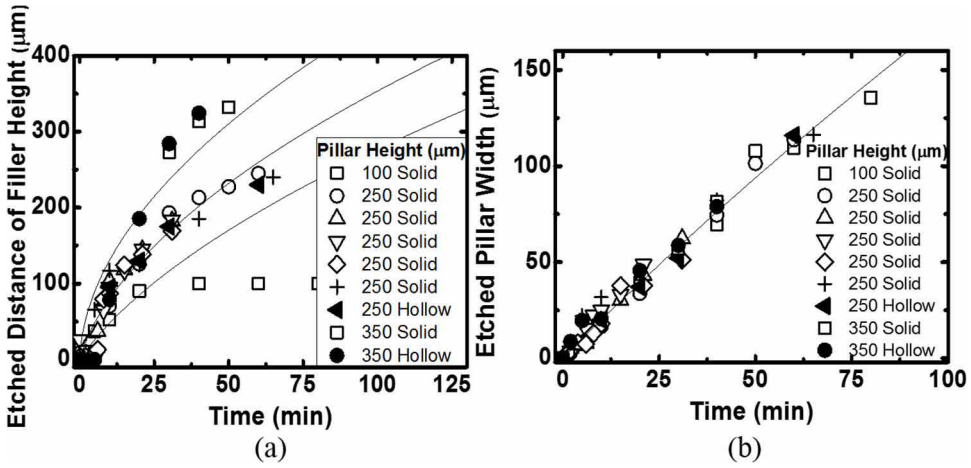

Figure 7. (a) The etched distance of filler height with respect to time; (b) etched pillar width with respect to time. The microneedles were all 160 μm in width and 1 mm apart from each other. The heights varied, but all etch was in the reaction-controlled regime. There were approximately 700 fillers of 10 μm in width surrounding a single pillar. The inner bore of the hollow microneedle was 40 μm in diameter. The 50 ml of HF (49 wt%)/HNO_3 (69 wt%) with volume ratio of 1:19 was used for etching 0.02 g of silicon, and 800 ml for etching silicon in a wafer scale. For 100 μm solid microneedle, the etch was terminated around 20 min as the fillers were all etched away. With diffusivity and reaction constants from table S1, we plotted the theoretical curves represented by solid lines (see section 3.4 for details).

(minimum of 50 ml) and a volume ratio of etchants (HF/HNO_3 at a 1/9 ratio versus 1/29 ratio). Thus, both the etchant volume and ratio must be precise and consistent each time to create the most repeatable results. During our study, we chose the overall etchant volume per silicon mass to be 800 mL for every 0.35 g of silicon and 1:19 (HF:HNO_3) for the etchant volume ratio because the relatively non-reactive etching that provides a moderate etch rate of 1 to 2 μm min^{-1} for sharpening the main pillar tip. The rich-HNO_3 system is also known to be more stable than the rich-HF solutions and is easily controllable, as the etchant lifetime is longer and rate constant of nitrite decomposition varies significantly less in temperature changes than the rich-HF solution as long as there is no physical agitation [39, 42].

3.2. Effect of hollow versus solid microneedle fabrication

Ideally, our parametric study can be performed using solid microneedles, since fabricating hollow microneedles requires three more fabrication steps. To prove that our etch conditions produce similar uniformity and geometric dimensions in both hollow and solid microneedles, we fabricated solid microneedles using the same conditions as shown in figures 1 and 2, but with pillar heights of 250 and 350 μm. Figure 7 shows deviation between the etch rates of the solid and the hollow microneedle, in which the pillar width and filler height deviated 4.32% and 3.77% respectively for hollow and solid microneedles of 350 μm in height, and 4.03% and 3.71% for 250 μm tall microneedles. Therefore, solid microneedles constituted the remainder of our parametric study.

3.3. Effect of wafer versus die-based fabrication

We fabricated solid microneedle arrays in a 13 mm × 13 mm die as well as a full wafer with the same geometric features and found that the pillar width and filler height from the full wafer scale fabrication deviated around 3% and 8% respectively in the

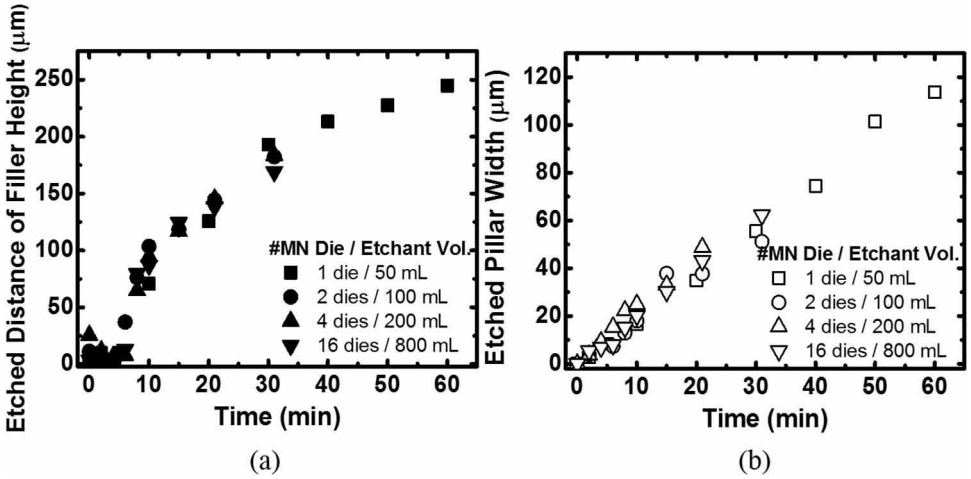

Figure 8. (a) The etched distance of filler height with respect to time (b) etched pillar width with respect to time. One die consisted an array of 13 × 13 microneedles of 160 μm in width and 250 μm in height that was 1 mm apart from each other. There were 700 fillers of 10 μm in width surrounding a single pillar. The etchant volume of HF (49 wt%): HNO_3 (69 wt%) in volume ratio of 1:19 was varied accordingly depending on the number of silicon die. One die is equivalent to 0.02 g of silicon. The filler height and pillar width of a full wafer had deviated 8.23%, and 2.98% respectively on average from the die scale fabrication. This non-uniformity rate may be due to a slight variation in the total etchant volume or mass of silicon.

same etch conditions from the die-scale fabrication (figure 8). Note that to match the silicon etchant volume, we performed experiments in 50 ml of HF and HNO_3 for a single die and 800 ml enchant for a full wafer. Given this similarity, the remainder of our parametric study is performed on single dies.

3.4. Effect of silicon microstructure geometries

To fabricate a very sharp needle, we must be able to accurately predict the lateral etch rate of the initial rectangular pillar (to make sure the pillar tip is sharpened) and vertical etch rate of the surrounding filler (to make sure the fillers are completely removed). Both of these requirements are highly dependent on the ratio of pillar pitch to pillar height, the initial filler surface area, and the initial filler density. For example, as the pillar pitch decreases, the slower both the lateral etch rate of the pillar and vertical etch rate of the filler will be due to the insufficient transfer of the fresh reagents from the bulk etchant to the silicon surface. To understand the intricate interplay of these parameters, we systematically adjusted pillar height, pillar pitch, filler surface area, and filler density to determine the etch regime (linear, nonlinear, reaction limited and/or mass transport limited), corresponding etch rate, and model with which to accurately predict the etch profile. To determine the various pillar and filler dimensions, we measured 9 needles on every four corners and center of a single square 13 mm × 13 mm die and averaged the values. In addition to analyzing 53 dies of different pillar height, pitch and surface area using SEM and confocal microscopy, we processed three silicon wafers with an identical fabrication procedure to evaluate and ensure repeatability.

One of the most important parameters that determine the etch regime is the pillar pitch to height ratio, or in other words, how close together the pillars are compared to how tall they are. Intuitively, the closer together and taller they are, the longer it will take reactants to reach the base of the pillars, consequently decreasing the etch rate. Specifically, we tested a die of microneedle arrays with different heights (100, 150, and 250 μm) and pitches (50, 100, 200, 400, 600, 800, and 1000 μm) and measured the lateral etch rate of the pillar. To keep the experiment well-controlled, the filler density remained relatively similar across all experiments, ranging from 5.7 to 8.0% filler density with respect to pitch area.

Results are shown in figure 9 and reveal two distinguishable regions based on the pillar pitch to height ratio. We note that when this ratio becomes larger than roughly 2 (figure 9(b)), we achieve a constant etch rate of pillar tip width, which suggests that the etch is not mass transport controlled, but reaction controlled. This is a predictable behavior as there is fresher etchant available at the etch front when the pillar pitch is large, allowing the etch rate to be constant for different geometries and not be restricted to the transport rate of the reagents. When the pillars are too close together (i.e. the pitch-height ratio is low), the etching process is relatively slow because there are less fresh reagents available to move through a stagnant film to the silicon surface.

We can describe this process more rigorously with a model similar to the Deal–Grove model. As the Deal–Grove model explains the growth of oxide on silicon due to the processes of (1) diffusing to the substrate and (2) reacting with the substrate, here we have reactants diffusing to the surface and then reacting to etch silicon dioxide (SiO_2). Specifically, when HF-HNO_3 is introduced into our silicon system, the substrate is oxidized, forming a SiO_2 surface. This oxide layer is consumed by fluoride ions [43, 44]. Despite the complexity of the etching process by HF-HNO_3, we can treat our system (rich-HNO_3) as one step reaction since the etch is limited by the dissolution of HF [43]. Here we assume that the steady state diffusive flux can be written as

$$J = -D\frac{\partial C}{\partial x} = J = D\frac{\partial (C_{\mathrm{b}} - C_{\mathrm{s}})}{\partial x} \qquad (1)$$

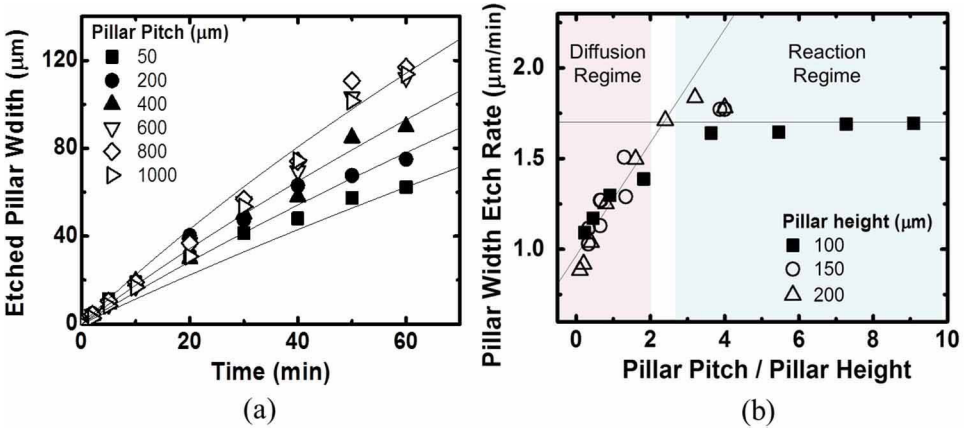

Figure 9. (a) The etched pillar width with respect to time for microneedle arrays of 250 μm in height. The lines represent the theoretical curve based on equation (1), with $D = 3.34 \times 10^{-9}$ m^2 s^{-1}, $k = 5.45 \times 10^{-6}$ m s^{-1}, and initial concentration ranging from 600 mol m^{-3} to 1300 mol m^{-3} depending on the pitch. (b) Etch rate of the pillar tip versus the ratio of pillar pitch to pillar height. At ratios below 2, the etch is mass transport limited, and etch rates are not constant with pitch to height ratio. As the ratio increases, the etch is reaction limited due to the large spacing between two pillars, and the etch rate is effectively constant.

where J is the diffusive flux of the fluoride ions, D is the diffusivity (m^2 s^{-1}), C_b is the bulk concentration of the reagents (mol m^{-3}), C_s is the concentration at the etching surface (mol m^{-3}), and δ is the distance traveled by the etching front (m). At the etch front, the chemical reagents are depleted and we assume the reactive flux is simply a first-order reaction:

$$J = kC_s \tag{2}$$

where k is the first order reaction rate constant (m s^{-1}). Equating the two fluxes, eliminating C_s, and neglecting higher order terms, the resulting flux is:

$$J = \frac{DkC_b}{\delta k + D} \tag{3}$$

which can be divided by moles of reactive species (HF) per volume (SiO_2) to show the etch movement as a function of time [45]. Accounting the boundary conditions of zero flux of reagents through the silicon nitride mask and assumptions of constant bulk concentration of the solution and constant etch rate and concentration at the reacting silicon surface, we achieve the following equation:

$$\delta(t) = -\frac{D}{k} + \sqrt{\left(\frac{D}{k}\right)^2 + (2DC_bAt)} \tag{4}$$

where A is the proportionality constant that accounts for molecular weight and density of the oxide layer; this equation takes the same form presented by Liu [46] and Westberg [47].

Our model values are shown alongside the measured data in figure 4. In the reaction-controlled regime, we chose C_b to be the true bulk concentration value of 1300 mol m^{-3}, and found the best fit for both k and D (values shown in table 1). As the overlap of the diffusion layer and proximity of the two adjacent pillars prohibit the bulk concentration from being the initial concentration at the etch front in the mass transport controlled regime, we chose a lower initial value of the bulk concentration in these cases. Specifically, with the best fit k and D parameters from the reaction controlled regime, we best fit the initial concentration in the diffusion regime, assuming a linear diffusive flux and constant chemical diffusivities and rate constants. Thus in these cases, we found the concentrations to be 600, 700, and 900 mol m^{-3} for the pillar pitch of 50, 200, and 400 μm respectively.

Table 1. Apparent reaction and diffusion constants for different etching models. We fit k and D values based on the experimental data from etching the array of pillars that are 160 μm in base width, 250 μm in height, and 50–1000 μm in pitch.

Fitting model	Apparent constants	Fitted parameters (1:19 = HF:HNO_3)
Diffusion	D (m^2 s^{-1})	3.34×10^{-9}
Linear fit	k (m/mol/s)	5.45×10^{-6}
Polynomial fit	k_1 (m/mol/s)	1.00×10^{-8}
Polynomial fit	k_2 (m^4/mol/s)	3.51×10^{-8}

Table 1 shows the results of our model. Literature shows that k is highly dependent on the geometry of the predefined structures and D is dependent on the etch chemistries, temperature, and viscosity [43]. Unfortunately, there is no literature values for our exact geometry, chemistry and etch bath conditions. However, for the mixture of HF (49%) and HNO_3 (69%) with a volume ratio of 1:9, the diffusivity constant from computational fit was roughly 1×10^{-9} m^2 s^{-1} [43]; thus, it is safe to assume that our diffusivity constant is within a reasonable range. Our k value is also acceptable, as Damkohler number ($kL/\alpha D$), where L is a characteristic length (height of pillar in this case) and α is a parameter that represents the pitch to height ratios (P/4H our case, see supplementary information figure S1 and table S1), agrees with our distinction of reaction-diffusion regimes. For example, when pillar pitch to height ratios are less than 2, Da is larger than 1, which indicate a diffusion limited system. This trend also applies for different pillar heights, as shown in supplementary information (figure S1 and table S1).

If the pillar pitch to height ratio is relatively large and there is no filler, the etchants will reach the bottom of the pillar, etching the base (at average of 5.62 ± 0.88 μm min^{-1} for a 200 μm tall microneedle etched in the reaction regime) to the detriment of the shape of the microneedle. Therefore, fillers are essential

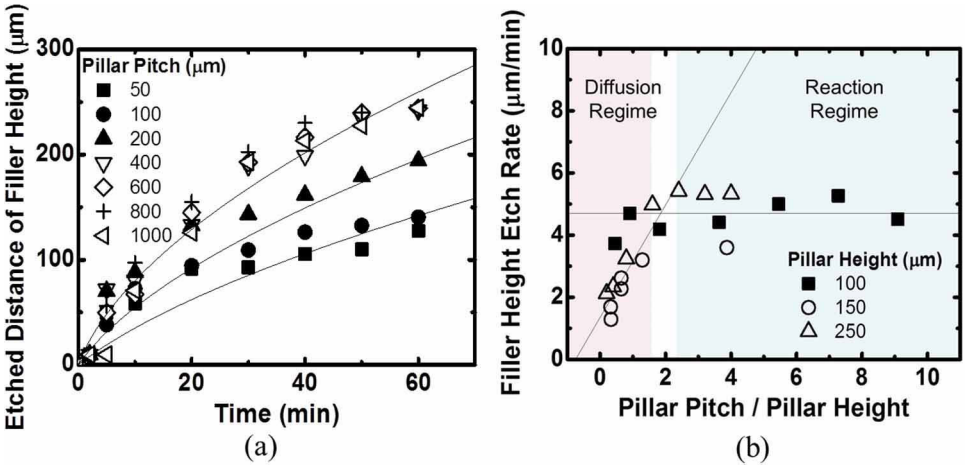

Figure 10. (a) The etched distance of filler height with respect to the etch time. Over time, the acid bath shortens the filler height as it sharpens the pillar tip (pillar height, however, remains constant due to masking by Si_3N_4). Data is superposed with a fit accounting for a reaction rate that includes both a linear (k_1) and quadratic term (k_2) to estimate the effective reaction constants ($k_1 = 1.00 \times 10^{-8}$ m/mol/s, $k_2 = 3.51 \times 10^{-8}$ m^4/mol/s, and $D = 3.34 \times 10^{-9}$ m^2 s^{-1}). (b) Similar to figure 4, when the pillar pitch to height ratio is approximately above 2, the etch dynamics are reaction limited and Da < 1, whereas below 2 is diffusion limited with Da > 1.

for achieving uniform and predictable final microneedle geometry because they can hinder the diffusion of reactive reagents from reaching and etching the pillar base. However, it is also important to etch the filler all the way to zero height exactly when the pillar tip is sharpened. Therefore, we performed a systematic study to understand the etch rate of the fillers based on filler density, surface area, pillar pitch, and pillar pitch to height ratio. Unlike the etch profile of the pillar width, the filler is shortened in a more nonlinear fashion (figure 10(a)). The reason for this is due to the competitive etching of the filler and the pillar. As the etchant dissolves the filler vertically, the distance for the reactive species to travel from the bulk etchant to the filler tip increases. As this distance increases, there is a decrease in the initial concentration of the fresh etchant and the etchant is thus scarcer towards the bottom of the trench. Comparatively, the pillar height remains relatively constant due to the silicon nitride mask on top, and there is no change in distance for the reagents to travel; thus, the pillar tip etches relatively linearly, while the filler height etches in more nonlinearly with respect to time. Similar to the lateral pillar etch, when the ratio of the pillar pitch to height is larger than 2, the fillers are etched in the reaction controlled regime, where the etch rate is constant for every pillar pitch to height ratio.

The Deal–Grove model can still describe the behavior of this etch but to accurately capture the dynamics of the filler etch, the reactive flux should contain chemical reaction rate constant that includes both a linear and quadratic term so that the reactive flux takes the form of:

$$J = k_1 C_s + k_2 C_s^2 \tag{5}$$

where k_1 is a first order reaction constant (m s^{-1}) and k_2 is a second order reaction constant (m^4/mol/s). We constructed the model and boundary conditions similar to the first order reaction model above (equations (1)–(4)), and the theoretical curves with respect to time are shown in figure 10, with values for k_1 and k_2 shown in table 1. These two constants are far smaller than the k value for the first-order system, which indicates that the reaction occurs faster when etching the pillar width than the filler height as there is easier access to fresh etchants and more chance for the molecular collisions to occur. The first-order reaction constant k is consistently larger than the combined first-and-second order constants k_1 and k_2 for various heights (250 μm shown in table 1, with others shown in SI).

Furthermore, it is important to note that even with these low k values for the reactive flux, the Da is still smaller than 1 in the reaction-controlled regime where the pillar pitch to height ratio is larger than 2, which confirms the validity of our fitting model and effective constants. For this case, we define the Damkohler number as:

$$\mathrm{Da} = \frac{kL}{D\alpha} = \left(\frac{k_1 + k_2 C_b}{2}\right)\frac{L}{D\alpha} \tag{6}$$

and α is (3P/4H)[3]. When this ratio is lower than 1, we enter the diffusion controlled regime, since there is simply not enough fresh reactants to physically reach the fillers as they are consumed by the neighboring pillars. In this case, the system is equivalent to a deep trench, in which the etch depth is larger than the pitch, and the arrival of the reagents to the reacting surface is the limiting step. Here, there is more competition to consume the reactive species in a vertical direction due to the proximity of the adjacent pillars near the fillers. In this diffusion regime, Da is calculated to be larger than 1 for every pitch to height ratio that is less than 2.

Filler density and surface area can also influence the lateral etch rate of the pillar and the vertical etch rate of the filler. For example, in a reaction-controlled regime, if the side surface area of the filler increases, then the filler volume etch rate increases in a moderately linear fashion (figure 11(a)) as the reaction is occurring immediately at the silicon surface. Furthermore, increasing filler density and filler width for a fixed pillar pitch can lead to a decrease in etch rate of the pillar width, as there is more silicon for the pillar to compete for consuming the reactive species (figure 11(b)).

In the diffusion regime, however, the etch rate is not constant for different pillar pitch to height ratios and increases

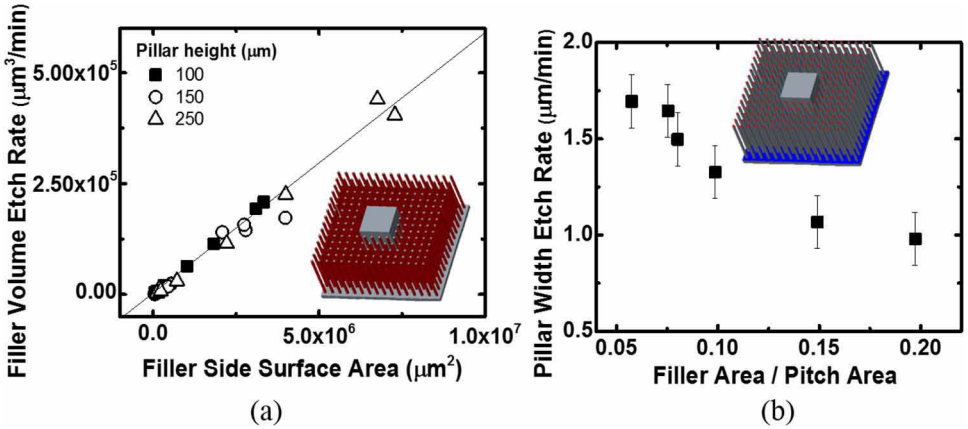

Figure 11. (a) The total volume etch rate of the fillers versus filler side surface area in the reaction regime. Since the fillers are etched nonlinearly, we measured the etch rate when the fillers were etched to 63% of original height. The filler width ranged from 9 to 17 μm, height from 100 to 250 μm, pitch from 200 to 1000 μm, pillar initial width 80 to 160 μm, and a number of surrounding fillers 200 to 800. The volume etch rate of the fillers increases with respect to the side surface area of the fillers because there is more surface area of the silicon substrate available for the reaction to occur. This applies to any fillers with different width, height, and density (pitch). The outliers are most likely due to the slight variation of the total etchant volume and mass of silicon (figure 8). The linear fit is $y = 0.0437x - 3207.3$ with $R^2 = 0.98$ (b) the etch rate of the pillar tip for different filler to pitch area ratio in the reaction-controlled etch regime. If the filler width and density increases for a certain pitch, the etch rate of the pillar will decrease since there are more fillers available nearby a single pillar that can hinder the etchant from being consumed at the pillar tip. The fitted curve is expressed as $y = -5.36x + 1.95$ with $R^2 = 0.92$.

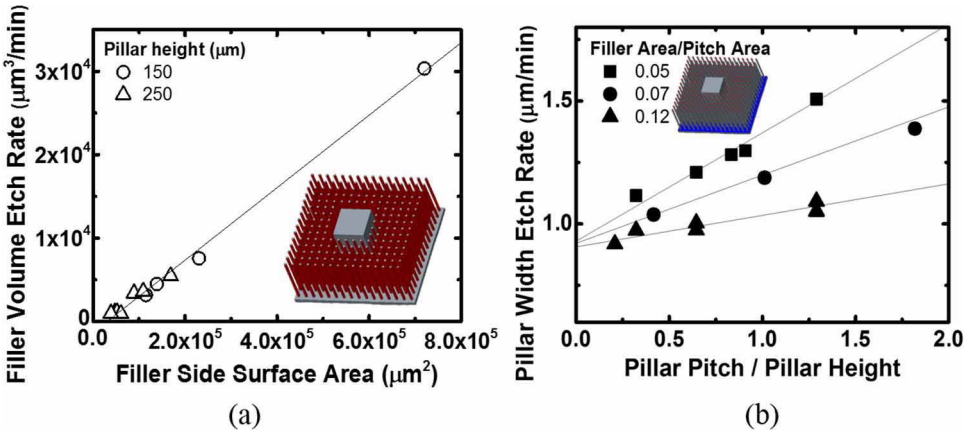

Figure 12. (a) The total volume etch rate of the fillers with respect to the filler side surface area in the diffusion regime. The filler width ranges from 9 to 17 μm, height from 150 to 250 μm, pitch from 50 to 200 μm, and initial filler width 80 to160 μm. In the diffusion regime, the etch rate of filler volume increases with respect to the filler side surface area for one single pillar, as in the reaction regime. The linear fit is $y = 0.044\,125x - 549.8$ with $R^2 = 0.97$ (b) the etch rate of the pillar tip for different pillar pitch to height ratios in the diffusion dominated etch regime. For a particular pitch to height ratio, the pillar width etch rate will decrease with respect to an increase of filler amount for a fixed pitch area. The linear fit trends are $y = 0.4016x + 0.961$ with $R^2 = 0.97$ for area ratio of 0.05, $y = 0.2494x + 0.9345$ with $R^2 = 1$ for area ratio of 0.07, and $y = 0.1179x + 0.9132$ and $R^2 = 0.89$ for area ratio of 0.12.

linearly as the pillars are placed farther away from one another, as seen in figures 9 and 10. Even for the same pillar pitch to height ratio, the pillar width etch rate can differ in the diffusion regime depending on the filler density (figure 12(b)). If the fillers are located close to each other, the etch rate of the pillar tip decreases as the active reagents have more silicon available to consume. Similar to the reaction controlled regime, the volume etch rate of the filler material increases as the surface area of the filler increases, since increased surface area leads to higher etch rates (figure 12(a)).

3.5. Design guidelines

Our parametric study shows that we can accurately model the etch rates of predefined structures using a rich-HNO_3 process and no agitation. Thus, we have developed a set of general design guidelines to create a wafer scale microneedle array with a controllable dimension, sharp microneedle tips, and high uniformity. For both diffusion and reaction regimes, fillers are required to make repeatable and reliable needles. For example, in the reaction controlled regime, when designing a mask for a microneedle array, the filler surface area should be 5 to 20% of the die without accounting for the pillar base area (figure 11(b)). This number can be arbitrary, but as the filler area increases, the etch rate of the pillar width decreases, since more fillers will need to be etched. With a chosen filler amount and the etch rates shown in figure 11(b), it is trivial to find the time required to sharpen the pillar given a base width. With this time, one can calculate the volume of filler required, and thus the volume etch rate for fillers. Then, from figure 11(a),

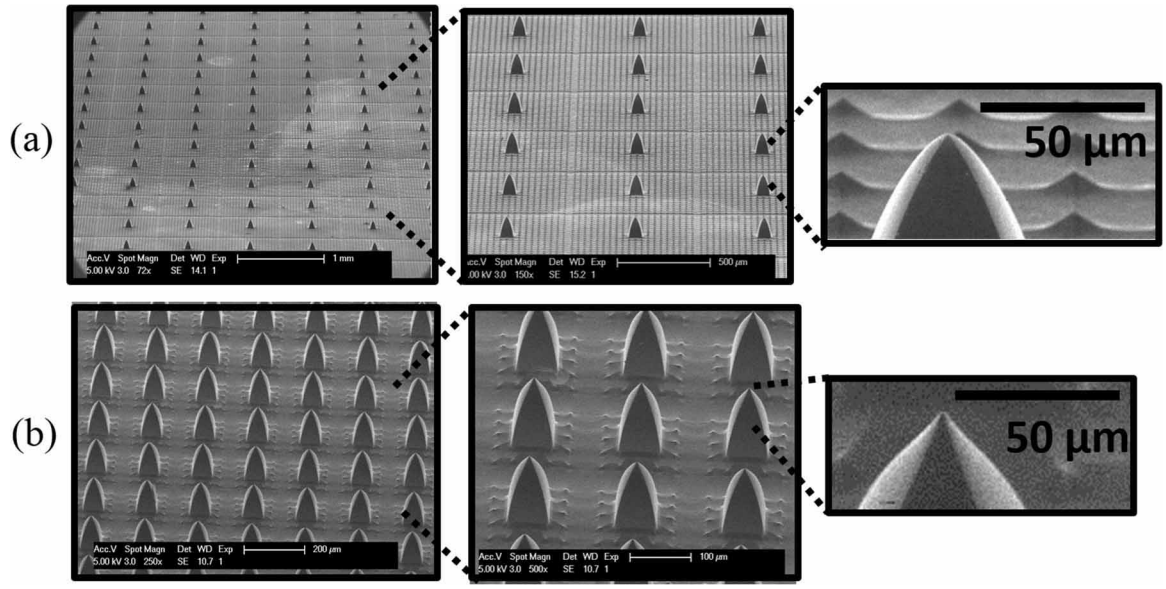

Figure 13. (a) SEM of an array of solid silicon microneedles in 13 mm × 13 mm die after etching in the HF-HNO_3 bath for 60 min. The starting pillar width was 80 μm, pitch 600 μm, and height 150 μm. (b) SEM of an array of solid silicon microneedles in 13 mm × 13 mm die after etching in the HF-HNO_3 bath for 65 min. The starting pillar width was 80 μm, pitch 100 μm, and height 150 μm.

the filler side surface area can be found, and with this number, one can easily design the filler density, width, and pitch. It should be noted that the filler pitch can range from 20 to 30 μm, and this distance does not affect the etch rate or profile. If designing microneedles that require etching in the diffusion limited regime, we must account for both filler amount and the pillar pitch to height ratio, since the etch rate is linearly dependent on the pillar pitch to height ratio (as opposed to being constant for the reaction regime). In this case, the selection of filler surface area and pillar width etch can be determined using figure 12(b).

As an alternative, the filler density and dimension can be designed using equations (7) and (8) for acquiring a desirable needle dimension, such as height, base width, and pitch in the reaction and diffusion regime respectively:

$$n = \frac{-27\,348.4p}{7.6708f^2h - fhp} \tag{7}$$

$$n = \frac{-1369.02\,p}{f(cf + 2.392\,93fh - 0.439\,492hp)} \quad \text{for 0.05 ratio of filler area to pitch area} \tag{8.1}$$

$$n = \frac{-2204.49\,p}{f(cf + 3.7469fh - 0.707\,69hp)} \quad \text{for 0.07 ratio of filler area to pitch area} \tag{8.2}$$

$$n = \frac{-4663.27\,p}{f(cf + 7.7455fh - 1.497\,03hp)} \quad \text{for 0.12 ratio of filler area to pitch area} \tag{8.3}$$

where p is the desirable microneedle base width, h is the microneedle height, c is the microneedle pitch, f is the width of fillers, and n is the number of fillers surrounding a single pillar that will become a microneedle in the end. Any arbitrary filler width can be used to find the filler density, as long as the ratio of filler area to pitch area is within 3% of the calculated area ratio. Note that equation (7) is a simplified version, in which the c term is neglected; this form is still acceptable, since equation (7) only applies to the reaction regime where the etch rate is constant for different ranges of the pitch to height ratio.

With the guidelines above, we successfully created an array of solid silicon microneedles for both reaction and diffusion limited regimes as shown in figures 13(a) and (b) respectively. For the reaction regime, we chose a filler width of 10 μm to obtain an array of microneedles with the width of 80 μm, height of 150 μm and pitch of 600 μm. After substituting these values in equation (7), we calculated the filler count to be 443 and thus placed exact 450 fillers of 10 μm in width surrounding a single 80 μm pillar. 450 fillers were chosen instead of 443 for a design symmetry, which is acceptable since the ratio of filler area to pitch area only deviates 1.5% from the calculated ratio. After etching the pillar array for approximately 60 min, we achieved the sharp microneedle array as shown in figure 13(a); the etch time can be predicted using figure 11, which is 59 min. As for the diffusion regime, we chose the filler area to be 5% of the pitch area and thus used equation (8.1) to obtain microneedles with base width of 80 μm, height 150 μm, and pitch of 100 μm. The filler count was calculated to be 16, and with our pillar pitch to height ratio, the corresponding pillar width etch rate was approximately 1.2 μm min^{-1} (figure 12(b)) with the expected etch time of 66 min. The final needle array is shown in figure 13(b). In both cases, we were able to achieve fabricate our initial design within our specifications of within 2% geometrical variation. Once the etch time came close to our predicted value, we inspected the pillar tip width under a microscope every minute to make sure the final pillar tip width was less than 5 μm; it should be noted that microneedles only need to have needle tip diameter of 15 μm or less to puncture human skin controllably [48].

4. Preliminary study on microneedle application

To demonstrate that our microneedles can penetrate skin or external medium, we manually pressed an array of 5 × 5

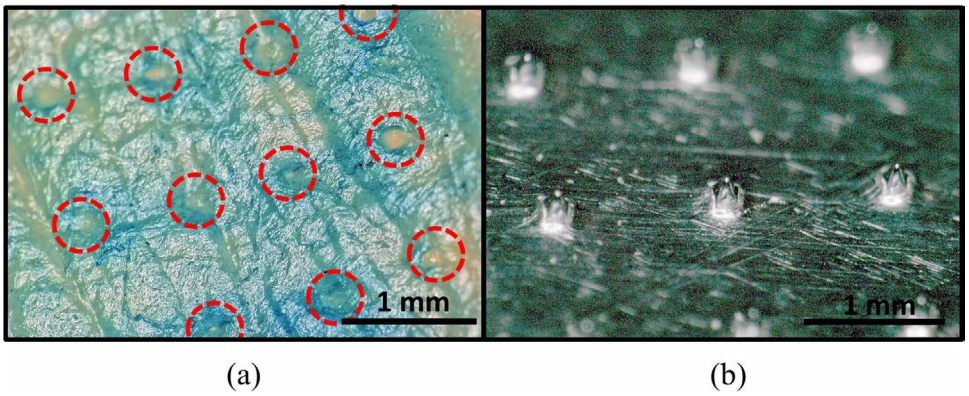

Figure 14. (a) Skin puncture marks observed on a chicken breast flesh with methylene blue staining. An array of microneedles with the base width of 160 μm, height 360 μm, and pitch 1 mm was used for the puncture test (b) microneedle piercing an aluminum foil, showing no damage after the application.

microneedles onto a piece of chicken breast, which has been used repeatedly as a biological simulation of human skin [49]. We applied blue dye to a surface pre-treated with microneedles with a base width 160 μm, height 360 μm, and pitch 1 mm. Figure 14(a) shows the array of puncture marks that are approximately 917.7 μm apart from each other, less than 1 mm due to the elastic nature of the biological tissue. After the application, we inspected the microneedles under a digital microscope (Keyence VHX 6000 Series, Keyence America, USA), in which we did not observe any mechanical failures. Furthermore, we pierced a 50 μm thick aluminum foil with the same microneedle arrays as shown in figure 14(b).

5. Conclusion

We fabricated uniform, repeatable, reliable hollow and sharp microneedle arrays with an HF-HNO_3 etch. The key to achieving such high uniformity is the non-agitated bath, the presence of silicon nitride masks, and surrounding filler material with well-defined geometries. We performed a parametric study with different predefined silicon geometries as well as the etch bath compositions to characterize the etch and theoretically verified the etch kinetics using a modified Deal–Grove model. From these data, we developed design guidelines for creating repeatable and reliable microneedle arrays with a pitch ranging from 100 μm to 1000 μm, height from 150 μm to 350 μm, inner bore diameter from 40 to 50 μm and base width from 80 to 160 μm. Specifically, once the needle array pitch, height, and base width are chosen, our models can guide the fabrication of microneedle arrays with specified amounts of filler density to create a sharp tip with less than 2% geometrical variation across the wafer. Because of the freedom of our design, we can thus fabricate dense hollow microneedle arrays to deliver drugs or monitor biomarkers transdermally, and/or produce individual hollow microneedles for single use applications. Our proposed method is non-labor intensive, well defined by theory, and straightforward for wafer scale mass production, opening doors to a plethora of potential medical and biosensing applications.

Acknowledgments

The authors acknowledge the CNSI Challenge Grant for initial funding for this work. H Kim was supported by the Institute for Collaborative Biotechnologies through Grants No. W911NF-09-D-0001 and No. W911NF-12-1-0031 through the U.S. Army Research Office, as well as the Errett-Fischer Foundation. The content of the information does not necessarily reflect the position of the policy of the government, and no official endorsement should be inferred. H Kim and S Pennathur are with the Department of Mechanical Engineering, University of California – Santa Barbara, Santa Barbara, 93106, USA. L S Theogarajan is with the Department of Electrical and Computer Engineering, University of California – Santa Barbara, Santa Barbara, 93106, USA.

ORCID iDs

S Pennathur https://orcid.org/0000-0003-2227-4005

References

[1] Cheung K and Das D 2014 Microneedles for drug delivery: trends and progress *Drug Deliv.* **23** 1–17
[2] Indermun S, Luttge R, Choonara Y, Kumar P, du Toit L, Modi G and Pillay V 2014 Current advances in the fabrication of microneedles for transdermal delivery *J. Control. Release* **185** 130–8
[3] Kim Y, Park J and Prausnitz M 2012 Microneedles for drug and vaccine delivery *Adv. Drug Deliv. Rev.* **64** 1547–68
[4] Kochba E, Levin Y, Raz I and Cahn A 2016 Improved insulin pharmacokinetics using a novel microneedle device for intradermal delivery in patients with type 2 diabetes *Diabetes Technol. Ther.* **18** 525–31
[5] Larrañeta E, Lutton R, Woolfson A and Donnelly R 2016 Microneedle arrays as transdermal and intradermal drug delivery systems: Materials science, manufacture and commercial development *Mater. Sci. Eng.* R **104** 1–32
[6] Anon 2014 Your solution for successful intradermal delivery Ondrugdelivery.com (www.ondrugdelivery.com/publications/49/Debiotech.pdf)
[7] Cormier M, Johnson B, Ameri M, Nyam K, Libiran L, Zhang D and Daddona P 2004 Transdermal delivery of

desmopressin using a coated microneedle array patch system *J. Control. Release* **97** 503–11
[8] Kim S and Roy S 2013 Microelectromechanical systems and nephrology: the next frontier in renal replacement technology *Adv. Chronic Kidney Dis.* **20** 516–35
[9] Martin F 2006 Method of producing tapered or pointed cannula *US Patent Specification* WO US 9675675 B2
[10] Zhang Y 2013 Microneedle device having a peptide therapeutic agent and an amino acid, methods of making and using the same *US Patent Specification* US 20140330198 A1
[11] Lin Y, Lee I, Hsu W, Hsu C, Chang K and Gao S 2016 Rapid fabrication method of a microneedle mold with controllable needle height and width *Biomed. Microdevices* **18** 85
[12] Wang M, Hu L and Xu C 2017 Recent advances in the design of polymeric microneedles for transdermal drug delivery and biosensing *Lab Chip* **17** 1373–87
[13] Takahashi H, Jung Heo Y, Arakawa N, Kan T, Matsumoto K, Kawano R and Shimoyama I 2016 Scalable fabrication of microneedle arrays via spatially controlled UV exposure *Microsyst. Nanoeng.* **2** 16049
[14] Takahashi H, Heo Y and Shimoyama I 2017 Scalable fabrication of PEGDA microneedles using UV exposure via a rotating prism *J. Microelectromech. Syst.* **26** 990–2
[15] Kim J, Kim M, Yang H, Lee K and Jung H 2013 Droplet-born air blowing: Novel dissolving microneedle fabrication *J. Control. Release* **170** 430–6
[16] Sullivan S, Murthy N and Prausnitz M 2008 Minimally invasive protein delivery with rapidly dissolving polymer microneedles *Adv. Mater.* **20** 933–8
[17] Bystrova S and Luttge R 2011 Micromolding for ceramic microneedle arrays *Microelectron. Eng.* **88** 1681–4
[18] Verbaan F, Bal S and van den Berg A 2008 Improved piercing of microneedle arrays in dermatomed human skin by an impact insertion method *J. Control. Release* **128** 80–8
[19] Mansoor I, Liu Y, Häfeli U O and Stoeber B 2013 Arrays of hollow out-of-plane microneedles made by metal electrodeposition onto solvent cast conductive polymer structures *J. Micromech. Microeng.* **23** 085011
[20] Norman J, Choi S, Tong N, Aiyar A, Patel S, Prausnitz M and Allen M 2012 Hollow microneedles for intradermal injection fabricated by sacrificial micromolding and selective electrodeposition *Biomed. Microdevices* **15** 203–10
[21] Park J, Allen M and Prausnitz M 2005 Biodegradable polymer microneedles: Fabrication, mechanics and transdermal drug delivery *J. Control. Release* **104** 51–66
[22] McAllister D, Wang P, Davis S, Park J, Canatella P, Allen M and Prausnitz M 2003 Microfabricated needles for transdermal delivery of macromolecules and nanoparticles: fabrication methods and transport studies *Proc. Natl Acad. Sci.* **100** 13755–60
[23] Khanna P, Luongo K, Strom J and Bhansali S 2010 Sharpening of hollow silicon microneedles to reduce skin penetration force *J. Micromech. Microeng.* **20** 045011
[24] Stoeber B and Liepmann D 2005 Arrays of hollow out-of-plane microneedles for drug delivery *J. Microelectromech. Syst.* **14** 472–9
[25] Mukerjee E, Collins S, Isseroff R and Smith R 2004 Microneedle array for transdermal biological fluid extraction and *in situ* analysis *Sensors Actuators* A **114** 267–75
[26] Ji J, Tay F and Miao J 2006 Microfabricated hollow microneedle array using ICP etcher *J. Phys.: Conf. Ser.* **34** 1132–6
[27] Griss P and Stemme G 2003 Side-opened out-of-plane microneedles for microfluidic transdermal liquid transfer *J. Microelectromech. Syst.* **12** 296–301
[28] Le-Thanh H, Tran-Minh N, Le The H and Karlsen F 2014 A study on mechanical strength of pyramid-shaped microneedle *2nd Middle East Conf. on Biomedical Engineering*
[29] Miller P, Narayan R and Polsky R 2016 Microneedle-based sensors for medical diagnosis *J. Mater. Chem.* B **4** 1379–83
[30] Olatunji O, Das D, Garland M, Belaid L and Donnelly R 2013 Influence of array interspacing on the force required for successful microneedle skin penetration: theoretical and practical approaches *J. Pharm. Sci.* **102** 1209–21
[31] Barnett A, Lee Y and Moore J 2015 Fracture mechanics model of needle cutting tissue *J. Manuf. Sci. Eng.* **138** 011005
[32] Jurčíček P, Zou H, Zhang S and Liu C 2013 Design and fabrication of hollow out-of-plane silicon microneedles *Micro Nano Lett.* **8** 78–81
[33] Chen P, Shih C and Tai Y 2006 Design, fabrication and characterization of monolithic embedded parylene microchannels in silicon substrate *Lab Chip* **6** 803
[34] Wilke N, Mulcahy A, Ye S and Morrissey A 2005 Process optimization and characterization of silicon microneedles fabricated by wet etch technology *Microelectron. J.* **36** 650–6
[35] Hamzah A, Abd Aziz N, Yeop Majlis B, Yunas J, Dee C and Bais B 2012 Optimization of HNA etching parameters to produce high aspect ratio solid silicon microneedles *J. Micromech. Microeng.* **22** 095017
[36] Negi S and Bhandari R 2012 Silicon isotropic and anisotropic etching for MEMS applications *Microsyst. Technol.* **19** 203–10
[37] Kulkarni M and Erk H 2000 Acid-based etching of silicon wafers: mass-transfer and kinetic effects *J. Electrochem. Soc.* **147** 176
[38] Bhandari R, Negi S, Rieth L and Solzbacher F 2010 A wafer-scale etching technique for high aspect ratio implantable MEMS structures *Sensors Actuators* A **162** 130–6
[39] Tuck B 1975 The chemical polishing of semiconductors *J. Mater. Sci.* **10** 321–39
[40] Kuiken H 2003 A mathematical model for wet-chemical diffusion-controlled mask etching through a circular hole *J. Eng. Math.* **45** 75–90
[41] Whitton J and Everall J 1973 The thickness of the epidermis *Br. J. Dermatol.* **89** 467–76
[42] Steinert M, Acker J, Oswald S and Wetzig K 2007 Study on the mechanism of silicon etching in HNO_3-rich HF/HNO_3 mixtures *J. Phys. Chem.* C **111** 2133–40
[43] Baranski M, Albero J, Kasztelanic R and Gorecki C 2011 A numerical model of wet isotropic etching of silicon molds for microlenses fabrication *J. Electrochem. Soc.* **158** D681
[44] Liu Z, Sun T, An J, Wang J, Xu X and Cui R 2007 Silicon etching in $HF/HNO_3/NH_3{\cdot}H_2O/H_2O$ system *J. Electrochem. Soc.* **154** D21
[45] Rath P, Chai J, Zheng H, Lam Y and Murukeshan V 2006 Total concentration approach for three-dimensional diffusion-controlled wet chemical etching *Int. J. Heat Mass Transfer* **49** 3408–16
[46] Liu J, Tai Y, Lee J, Pong K, Zohar Y and Ho C 1993 *In situ* monitoring and universal modelling of sacrificial PSG etching using hydrofluoric acid *Proc. IEEE Micro Electro Mech. Syst.* pp 71–6
[47] Westberg D, Paul O, Andersson G and Baltes H 1996 Surface micromachining by sacrificial aluminium etching *J. Micromech. Microeng.* **6** 376–84
[48] Römgens A, Bader D, Bouwstra J, Baaijens F and Oomens C 2014 Monitoring the penetration process of single microneedles with varying tip diameters *J. Mech. Behav. Biomed. Mater.* **40** 397–405
[49] Zhang P, Dalton C and Jullien G 2009 Design and fabrication of MEMS-based microneedle arrays for medical applications *Microsyst. Technol.* **15** 1073–82